Supporting Information

Lai et al. 10.1073/pnas.1715851115

Analysis of the Bulk Spectrum

In the strong coupling regime that is relevant to heavy-fermion systems, we can approach the prohibition of d_σ fermion double occupancy by an auxiliary boson method (1). Representing $d^\dagger_{i\sigma} = f^\dagger_{i\sigma} b_i$, the $f^\dagger_{i\sigma}$ (b_i) are fermonic (bosonic) operators satisfying the constraint $b^\dagger_i b_i + \sum_\sigma f^\dagger_{i\sigma} f_{i\sigma} = 1$. At the saddle-point level, we replace $b^\dagger_i,\ b_i \to r$ and introduce a Lagrange multiplier ℓ to enforce the local constraint. Defining $\Xi^T_{\mathbf{k}} \equiv \left(d_{k\uparrow,A}\ \ d_{k\uparrow,B}\ \ d_{k\downarrow,A}\ \ d_{k\downarrow,B}\right)$ and $\Psi^T_{\mathbf{k}} \equiv \left(c_{k\uparrow,A}\ \ c_{k\uparrow,B}\ \ c_{k\downarrow,A}\ \ d_{k\downarrow,B}\right)$, we can transform Hamiltonian H_c, H_{cd}, and H_d into the pseudospin basis using $\breve{\Xi}_{\mathbf{k}} = S^\dagger_\sigma \Xi_k$ and $\breve{\Psi}_{\mathbf{k}} = S^\dagger_\sigma \Psi_k$, with $S^\dagger_\sigma = U_\sigma \tau_0$ being a unitary matrix which consists of the $|\pm D\rangle$ eigenvectors. The effective hybridization becomes rV, which is nonzero only for $V > V_c$, whenever the conduction-electron density of states has a pseudogap form near the Fermi energy (2). The hybridization part can be reexpressed as

$$H_{cd} = \sum_{\mathbf{k}} \left[\breve{\Psi}^\dagger_{\mathbf{k}} \cdot rV \mathbb{1}_4 \cdot \breve{\Xi}_{\mathbf{k}} + \text{H.c.}\right]. \qquad \text{[S1]}$$

Introducing $\breve{\Psi}^T_{\mathbf{k}} = \left(\breve{\psi}^T_{k+}\ \ \breve{\psi}^T_{k-}\right)$, $\breve{\Xi}^T_{\mathbf{k}} = \left(\breve{\xi}^T_{k+}\ \ \breve{\xi}^T_{k-}\right)$, where $\breve{\psi}^T_{k\pm} = \left(\breve{\psi}_{k\pm,A}\ \ \breve{\psi}_{k\pm,B}\right)$ and $\breve{\xi}^T_{k\pm} = \left(\breve{\xi}_{k\pm,A}\ \ \breve{\xi}_{k\pm,B}\right)$, we find that the strong-coupling Hamiltonian can straightforwardly be written in the $|\pm D\rangle$ basis as $H^s = \sum_{a=\pm} \mathcal{H}^s_a$,

$$\mathcal{H}^s_a = \sum_{k,a=\pm} \begin{pmatrix}\breve{\psi}^\dagger_{ka} & \breve{\xi}^\dagger_{ka}\end{pmatrix} \begin{pmatrix} h_{ka} - \mu \mathbb{1}_2 & V_s \mathbb{1}_2 \\ V_s \mathbb{1}_2 & E_s \mathbb{1}_2 \end{pmatrix} \begin{pmatrix}\breve{\psi}_{\mathbf{k}a} \\ \breve{\xi}_{\mathbf{k}a}\end{pmatrix}, \qquad \text{[S2]}$$

where $V_s \equiv rV$ and $E_s \equiv E_d + \ell$. Straightforward diagonalization of the strong-coupling Hamiltonian yields a set of four quasiparticle bands for each spin sector as

$$\mathcal{E}^{(\tau,\alpha)}_{\pm D}(k) = \frac{1}{2}\left[E_s + \tilde{\varepsilon}^\tau_{\pm D} + \alpha\sqrt{\left(E_s - \tilde{\varepsilon}^\tau_{\pm D}\right)^2 + 4V_s^2}\right], \qquad \text{[S3]}$$

$$\tilde{\varepsilon}^\tau_{\pm D} = \varepsilon^\tau_{\pm D} - \mu, \qquad \text{[S4]}$$

$$\varepsilon^\tau_{\pm D} = \tau\sqrt{u_1(k)^2 + u_2(k)^2 + (m \pm \lambda D(k))^2}, \qquad \text{[S5]}$$

where $\tau = (+,-)$, and $\alpha = (+,-)$ indexes the upper/lower quartet of bands, respectively.

To gain a deeper understanding of the gap structure of the hybridized bands, it is more convenient to first diagonalize the conduction electron part of the Hamiltonian, which is possible since the off-diagonal blocks and the bottom right block are all proportional to 2×2 identity matrices. Diagonalizing the conduction electron part of the Hamiltonian, we can rewrite the strong coupling Hamiltonian in a diagonal form,

$$h^D_{k\pm} = \begin{pmatrix} \varepsilon^+_{\pm D} & 0 \\ 0 & \varepsilon^-_{\pm D}\end{pmatrix}, \qquad \text{[S6]}$$

and in the new basis, the Hamiltonian becomes

$$\mathcal{H}^s_\pm = \sum_k \begin{pmatrix}(\psi^D_{k\pm})^\dagger & (\xi^D_{k\pm})^\dagger\end{pmatrix} \begin{pmatrix} h^D_{ka} - \mu\mathbb{1}_2 & V_s\mathbb{1}_2 \\ V_s\mathbb{1}_2 & E_s\mathbb{1}_2\end{pmatrix} \begin{pmatrix}\psi^D_{\mathbf{k}\pm} \\ \xi^D_{\mathbf{k}\pm}\end{pmatrix}. \qquad \text{[S7]}$$

We can then directly see that the matrix elements associated with the first and third fields are decoupled from the second and fourth fields, which means we can simplify the 4×4 matrix in either $|\pm D\rangle$ sector, to be two 2×2 matrices, which allows us to examine the eigenenergy bands analytically. Below, we discuss the cases in different $|\pm D\rangle$ sectors separately. Our main conclusion below is that the WKSM phase can only occur at the $|-D\rangle$ sector in the hybridized band regime, and the hybridized bands in $|+D\rangle$ sector always remain gapped.

$|+D\rangle$ sector:

For further analysis in the band gaps, we assume that E_s lies well below the conduction electron bands $\varepsilon^\tau_{\pm D}$. In addition, for the condition for 1/4-filling, E_s is required to be positive $E_s > 0$. Focusing on the two 2×2 matrices of the $|+D\rangle$ sector, we can separate the Hamiltonian into $\mathcal{H}^s_+ = \sum_{\alpha,\tau} H^{s,\tau}_{+,\alpha}$, the energies obtained are

$$\mathcal{E}^{(+,\alpha)}_{+D} = \frac{1}{2}\left[E_s + \tilde{\varepsilon}^+_{+D} + \alpha\sqrt{\left(E_s - \tilde{\varepsilon}^+_{+D}\right)^2 + 4V_s^2}\right] \qquad \text{[S8]}$$

$$\mathcal{E}^{(-,\alpha)}_{+D} = \frac{1}{2}\left[E_s + \tilde{\varepsilon}^-_{+D} + \alpha\sqrt{\left(E_s - \tilde{\varepsilon}^-_{+D}\right)^2 + 4V_s^2}\right]. \qquad \text{[S9]}$$

Since $\varepsilon^+_{+D} > \varepsilon^-_{+D}$, we can see $\mathcal{E}^{(+,+)}_{+D} > \mathcal{E}^{(-,-)}_{+D}$ and these two bands always remain gapped. Similarly, within each pair of branches $\mathcal{E}^{(\tau,+)}_{+D} > \mathcal{E}^{(\tau,-)}_{+D}$, and they should be always gapped. The only possibility that the gap closes occurs between $\mathcal{E}^{(+,-)}_{+D}$ and $\mathcal{E}^{(-,+)}_{+D}$. If there is a crossing between them at some momenta $k = \mathbf{k}_0$, the two bands should be degenerate $\mathcal{E}^{(+,-)}_{+D}(\mathbf{k}_0) = \mathcal{E}^{(-,+)}_{+D}(\mathbf{k}_0)$, which leads to

$$\begin{aligned}\varepsilon^+_{+D}(\mathbf{k}_0) - \varepsilon^-_{+D}(\mathbf{k}_0) &= \sqrt{\left(E_s - \tilde{\varepsilon}^+_{+D}(\mathbf{k}_0)\right)^2 + 4V_s^2} \\ &\quad + \sqrt{\left(E_s - \tilde{\varepsilon}^-_{+D}(\mathbf{k}_0)\right)^2 + 4V_s^2} \\ &\geq \varepsilon^+_{+D}(\mathbf{k}_0) + \varepsilon^-_{+D}(\mathbf{k}_0) - 2E_s \\ &\Rightarrow \varepsilon^-_{+D}(\mathbf{k}_0) \leq E_s, \end{aligned} \qquad \text{[S10]}$$

where we use the assumption that $E_s < \varepsilon^\tau_{\pm D}$ in the second line. This in turn leads to a contradiction to our initial condition that the d fermion Fermi energy is well below the four conduction electron bands, $E_s < \varepsilon^\tau_{\pm D}$. Therefore, we conclude that there cannot be any crossing between $\mathcal{E}^{(+,-)}_{+D}$ and $\mathcal{E}^{(-,+)}_{+D}$. The hybridized bands in the $|+D\rangle$ sector always remain gapped at any momenta and Weyl nodes cannot reside there. Now let's examine the $|-D\rangle$ sector.

$|-D\rangle$ sector:

In the $|-D\rangle$ sector, we can also decompose the 4×4 Hamiltonian matrix to two 2×2 matrices, $\mathcal{H}^s_+ = \sum_{\alpha,\tau} H^{s,\tau}_{+,\alpha}$, which gives the eigenvalues as

$$\mathcal{E}^{(+,\alpha)}_{-D} = \frac{1}{2}\left[E_s + \tilde{\varepsilon}^+_{-D} + \alpha\sqrt{\left(E_s - \tilde{\varepsilon}^+_{-D}\right)^2 + 4V_s^2}\right], \qquad \text{[S11]}$$

$$\mathcal{E}^{(-,\alpha)}_{-D} = \frac{1}{2}\left[E_s + \tilde{\varepsilon}^-_{-D} + \alpha\sqrt{\left(E_s - \tilde{\varepsilon}^-_{-D}\right)^2 + 4V_s^2}\right]. \qquad \text{[S12]}$$

The bands' dispersions associated with the conduction electrons show Weyl nodes at certain momenta, i.e., $k = \mathbf{k}_W$, where $\varepsilon^+_{-D}(\mathbf{k}_W) = \varepsilon^-_{-D}(\mathbf{k}_W) = 0$. There are actually 12 inequivalent $\mathbf{k}_W$ along the $X - W$ lines on the 3D BZ boundary, determined by the condition $\frac{m}{4|\lambda|} = \sin(\frac{\mathbf{k}_0}{2})$, where $\mathbf{k}_W$ is a cyclic permutation of the elements in a vector $(\mathbf{k}_0, 0, \pm 2\pi)$. At $k = \mathbf{k}_W$, in the hybridized bands we then have

$$\mathcal{E}^{(+,+)}_{-D}(\mathbf{k}_W) = \mathcal{E}^{(-,+)}_{-D}(\mathbf{k}_W), \qquad \text{[S13]}$$

$$\mathcal{E}^{(+,-)}_{-D}(\mathbf{k}_W) = \mathcal{E}^{(-,-)}_{-D}(\mathbf{k}_W). \qquad \text{[S14]}$$

We can see that in the hybridized bands, there are actually two pairs of degenerate bands sitting at the momenta $\mathbf{k}_W$. Near $\mathbf{k}_W$, the band dispersions can be linearized.

Due to the constraints in the strong-coupling regime, $\mathcal{H}_a^s$ must be solved self-consistently with the saddle-point equations,

$$\begin{aligned}&\frac{1}{2N_u}\sum_{\mathbf{k},a=\pm}\left\langle \breve{\xi}^{\dagger}_{\mathbf{k}a}\breve{\xi}_{\mathbf{k}a}\right\rangle + r^2 = 1,\\ &\frac{V}{4N_u}\sum_{\mathbf{k},a=\pm}\left[\left\langle \breve{\psi}^{\dagger}_{\mathbf{k}a}\breve{\xi}_{\mathbf{k}a}\right\rangle + \text{H.c.}\right] + r\ell = 0,\end{aligned} \qquad \textbf{[S15]}$$

where N_u is the number of the unit cell. Here, we can tune the chemical potential to be $\mu = -V_s^2/E_s$, with $E_s > 0$. This fixes the lower Weyl node to the Fermi energy, at 1/4-filling, as shown in Fig. 2. For the illustration in the main text, we use the same bare coupling parameters to be $(t, \lambda, E_d, V) = (1, 0.5, 1, -6, 6.6)$, and solved self-consistently for $r \simeq 0.259$ and $\ell \simeq 6.334$, with error $\epsilon \leq \mathcal{O}(10^{-5})$ on a $64 \times 64 \times 64$ unit cell diamond lattice.

Berry Curvature

The Berry curvature field $\vec{\Omega}(k)$ is akin to a fictitious magnetic field in momentum space; analogously, the Weyl nodes manifest as monopole sources and sinks of Berry curvature (3, 4). The field is a way of representing the tensor components since it is a 3×3 antisymmetric tensor in 3D, $\vec{\Omega}(k) = (\Omega_{yz}(k), \Omega_{zx}(k), \Omega_{xy}(k))$. The components are given by the gauge invariant equation (3, 4),

$$\Omega_{ab}(k) = \sum_{n\neq n'} \mathcal{I}m \frac{\langle nk|\partial_{c,\mathbf{k}_a} H^s_{\mathbf{k}}|n'k\rangle\langle n'k|\partial_{c,\mathbf{k}_b} H^s_{\mathbf{k}}|nk\rangle}{(\mathcal{E}_n - \mathcal{E}_{n'})^2}, \qquad \textbf{[S16]}$$

where $H^s_{\mathbf{k}}$ is the 8×8 Bloch matrix in the strong coupling regime in physical spin space, $\partial_{c,\mathbf{k}_a}$ is the derivative with respect to only the conduction electrons corresponding to the velocity of the charge carriers. $\mathcal{E}_n = \mathcal{E}_\nu^{(\tau,\alpha)}$ and $|nk\rangle$ are the Bloch eigen energies and eigenstates of $H^s_{\mathbf{k}}$, with index n specifying one of the eight bands, $n = (\tau, \alpha, \nu) = (\pm, \pm, \pm D)$.

In the main text, the Berry curvature of the heavy Weyl fermions in the strong coupling regime were shown; specifically, we plot the field's unit length 2D projection onto the $\mathbf{k}_x$-$\mathbf{k}_y$ plane,

$$\begin{aligned}\hat{\Omega}(\mathbf{k}_x, \mathbf{k}_y, 2\pi) = &\frac{1}{|\vec{\Omega}(\mathbf{k}_x, \mathbf{k}_y, 2\pi)|}\\ &\times \left(\Omega_{yz}(\mathbf{k}_x, \mathbf{k}_y, 2\pi),\ \Omega_{zx}(\mathbf{k}_x, \mathbf{k}_y, 2\pi)\right).\end{aligned} \qquad \textbf{[S17]}$$

Surface States

Following the approach in ref. 5, we also seek surface states in the $|-D\rangle$ sector near the Weyl nodes. The nodes are on the square faces of the fcc BZ boundary, along the lines connecting high symmetry points X and W. We find that the Hamiltonian matrix of $\mathcal{H}^s_-$, Eq. **S2** can be expressed

$$\begin{aligned}h_-(\mathbf{k}) = &(\kappa^0 + \kappa^z) \otimes \tfrac{1}{2}\left[u_1(\mathbf{k})\tau_x + u_2(\mathbf{k})\tau_y + (m - \lambda D(\mathbf{k}))\tau_z\right]\\ &+ \left[(E_s - \mu)\kappa^0 - (E_s + \mu)\kappa^z + V_s\kappa^x\right] \otimes \tau_0\end{aligned} \qquad \textbf{[S18]}$$

where κ^i are Pauli matrices acting on the $\left(\breve{\psi}_{k-}, \breve{\xi}_{k-}\right)$ basis. We linearize the Hamiltonian matrix near $\mathbf{q} = \left(k_x, k_y, 2\pi\right)$ in $\tilde{q}_z = k_z - 2\pi$ around $\tilde{q}_z = 0$. Defining $u' \equiv \sqrt{(u'_1)^2 + (u'_2)^2}$, and $u \equiv \sqrt{u_1^2 + u_2^2}$, we obtain

$$\begin{aligned}h_-(\mathbf{q}) = &(\kappa^0 + \kappa^z) \otimes \tfrac{1}{2}[\tilde{q}_z u'(q)\tau_x - u(\mathbf{q})sgn(k_x k_y)\tau_y\\ &+ (m - \lambda D(\mathbf{q}))\tau_z] + \left[(E_s - \mu)\kappa^0\right.\\ &\left.-(E_s + \mu)\kappa^z + V_s\kappa^x\right] \otimes \tau_0.\end{aligned} \qquad \textbf{[S19]}$$

Making the real-space replacement $\tilde{q}_z \to -i\partial_z$, we can enforce the boundary condition by assigning the value of the staggered mass to be $m = m_+ > 4|\lambda|$ outside for $z > 0$ (trivially insulating vacuum), and $m = m_- < 4|\lambda|$ for $z < 0$, such that the bulk is in a stable Weyl semimetal phase.

Generalizing the wave function suggested in ref. 5, we find the surface eigenstates in the plane of the four Weyl nodes around the X point to be

$$\psi_s(k_x, k_y, z) = A_s e^{\mp \frac{z}{\xi_\pm}} |\kappa\rangle \otimes |\tau_y = +1\rangle \otimes |-D\rangle, \qquad \textbf{[S20]}$$

with

$$|\kappa\rangle = B_s \begin{pmatrix} 1 \\ -\sqrt{1 - \left(\frac{\beta^s_{\mathbf{k}}}{V_s}\right)^2} - \frac{\beta^s_{\mathbf{k}}}{V_s} \end{pmatrix}, \qquad \textbf{[S21]}$$

$$\beta^s_{\mathbf{k}} \equiv -\frac{1}{2}\left[u(\mathbf{q})sgn(k_x k_y) + E_s + \mu\right], \qquad \textbf{[S22]}$$

where A_s, B_s are normalization constants. We identify $\xi_\pm = \pm u'(\mathbf{q})/(m_\pm - \lambda D(\mathbf{q}))$ as the penetration depth of the surface wave functions. Inside the boundary, the divergence of ξ_- when $D(\mathbf{q}) = m_-$ indicates that the surface states merge with the bulk states, becoming indistinguishable (5).

Inversion-Symmetry Breaking and Time-Reversal-Symmetry Breaking Cases

Here, we consider H_c in the presence of a static magnetic field, as an illustration of the effect of a time-reversal symmetry breaking (TRB) on the Weyl state. Consider the conduction electron Hamiltonian,

$$H_c = \sum_{\langle ij\rangle,\sigma}\left(t_{ij}\, c^\dagger_{i\sigma} c_{j\sigma} + \text{H.c.}\right) + i\lambda \sum_{\langle\langle ij\rangle\rangle}\left[c^\dagger_{i\sigma}\left(\boldsymbol{\sigma}\cdot\mathbf{e}_{ij}\right) c_{j\sigma} - \text{H.c.}\right] \qquad \textbf{[S23]}$$

$$+ m\sum_{i,\sigma}(-1)^i c^\dagger_{i\sigma} c_{i\sigma} + \sum_j \boldsymbol{M}\cdot\left(c^\dagger_{j\sigma}\boldsymbol{\sigma} c_{j\sigma}\right) \qquad \textbf{[S24]}$$

where $e_{ij} = \frac{e_i \times e_j}{|e_i \times e_j|}$ are determined by the two bond vectors connecting second-nearest-neighbors, and $\boldsymbol{\sigma} = (\sigma_x, \sigma_y, \sigma_z)$ are the Pauli matrices acting on spin space, and the last term is the TRB term, with $\boldsymbol{M}$ being the local moment and $c^\dagger_{j\sigma}\boldsymbol{\sigma} c_{j\sigma}$ being the conduction electron spin.

The noncentrosymmetric diamond lattice (the "zincblende" lattice) is presented in Fig. S1*A*. Although the diamond and zincblende lattices are structurally the same, the different on-site potential m reduces the O_h cubic point group symmetry of the diamond lattice to tetragonal T_d symmetry in the zincblende. The simplest way to visualize the inversion symmetry-breaking introduced by the m term is to compare the interlocked sublattice unit cells under the inversion operations in Fig. S1*B*. If one reflects the position of any site across the indicated inversion center X, the upper four sites neatly exchange positions with the lower four. Conversely, if the on-site potential differentiates the sublattices via m, an inversion operation exchanges the distinct sublattice sites, as seen in Fig. S1*C*, so the inversion symmetry is broken.

Here, we show an example of a Weyl semimetal phase in the broken time reversal symmetry ($\boldsymbol{M} \neq 0$), in the case of the diamond lattice ($m = 0$). For simplicity, below we choose $\boldsymbol{M} = M_z\hat{z}$, and the second term becomes a Zeeman-like term. Following the same procedure as before, we introduce the basis in momentum space $\Psi^T_{\mathbf{k}} = \left(c_{\mathbf{k}\uparrow,A}\ \ c_{\mathbf{k}\uparrow,B}\ \ c_{\mathbf{k}\downarrow,A}\ \ c_{\mathbf{k}\downarrow,B}\right)$.

The Hamiltonian of the conduction electron becomes $H_{c,M}^{TRB} = \Psi_{\mathbf{k}}^{\dagger} \cdot h_c^{TRB} \cdot \Psi_{\mathbf{k}}$, with

$$h_c^{TRB} = \sigma_0 \left[u_1(\mathbf{k})\tau_x + u_2(\mathbf{k})\tau_y\right] + M_z\sigma_z\tau_0 + \lambda\left[\mathbf{D}(\mathbf{k})\cdot\boldsymbol{\sigma}\right]\tau_z, \quad \textbf{[S25]}$$

where $u_{1/2}$ and vector $\mathbf{D}$ are defined in the main text. A 3D Dirac semimetal is realized with Dirac points located at X points in the absence of the TRB term, as illustrated in Fig. S2*A*.

Upon increasing the TRB term, first we observe that Weyl nodes appear along $X-\Gamma$ lines and along $X-W$ lines on the 3D BZ boundary parallel to $\hat{\mathbf{k}}_z$-axis, and increasing to $M_z = 3$ moves both Weyl nodes toward the Γ point, illustrated in Fig. S2*B*.

Next, we analyze the critical value of M_z signaling the phase transition that separates the aforementioned TRB-Weyl semimetals from the topologically trivial insulator phase. Focusing on one of the $X-\Gamma$ lines that we suspect to harbor Weyl nodes, we assume its position is at $\mathbf{k}_W = \mathbf{k}_X - \delta\mathbf{k}$, where $\mathbf{k}_X$ is the X-point momentum, and $\delta\mathbf{k} = (\delta k_x, 0, 0)$ with $|\delta k_x| > 0$. We can then straightforwardly find that all of the components of $\mathbf{D}(\mathbf{k})$ along that line vanish. The Hamiltonian matrix along the line can be simplified to be

$$h_c^{TRB}|_{X\Gamma} = 2t\sigma_0\left[\left(1-\cos\left(\frac{\delta k_x}{2}\right)\right)\tau_x + \sin\left(\frac{\delta k_x}{2}\right)\tau_y\right] + M_z\sigma_z\tau_0,$$

which leads to the eigenvalues

$$E_c^{TRB,\sigma} = \sigma M_z \pm 2\sqrt{2\left[1-\cos\left(\frac{\delta k_x}{2}\right)\right]}, \quad \textbf{[S26]}$$

where $\sigma = \pm$ for spin $=\uparrow,\downarrow$. For $M_z > 0$, we can see that gaplessness can only occur when $M_z = 2\sqrt{2\left[1-\cos\frac{\delta k_x}{2}\right]}$, which leads to the condition

$$\cos\left(\frac{\delta k_x}{2}\right) = 1 - \frac{M_z^2}{8}. \quad \textbf{[S27]}$$

Therefore, we can see that the condition can be satisfied for $0 < M_z \le M_z^c = 4$, after which the absolute value of the right-hand side becomes >1 and the condition can no longer be held. The critical value of $M_z^c = 4$ is fully consistent with the numerical analysis illustrated in Fig. S2.

Specific Heat from a Weyl Node

The specific heat is calculated as

$$c_v = \left(\frac{\partial u}{\partial T}\right)_V = \frac{\partial}{\partial T}\int_{BZ}\frac{d^3\mathbf{k}}{(2\pi)^3}\varepsilon_{\mathbf{k}} f(\varepsilon_{\mathbf{k}}), \quad \textbf{[S28]}$$

where $\varepsilon_{\mathbf{k}}$ is the energy dispersion, u is the energy density, and the integral is over the first BZ. Here, the occupation distribution function $f(\varepsilon_{\mathbf{k}})$ is the Fermi function. We focus on the linear dispersion regime where we can approximate $\varepsilon_{\mathbf{k}} = \hbar v^* k$. We will take the renormalized Fermi velocity v^* for its asymptotic low-temperature value. Analyzing the temperature dependence of the condensate amplitude in our saddle-point analysis will only cause subleading corrections to the temperature dependence of the specific heat.

The result for the specific heat per unit volume is

$$c_v = \frac{7\pi^2}{30}k_B\left(\frac{k_B T}{\hbar v^*}\right)^3. \quad \textbf{[S29]}$$

This shows that the T^3 contribution to the specific heat becomes large when v^* is small, as in the case of heavy-fermion systems.

In the above calculation, we have assumed that the leading term of the specific heat at low temperatures is independent of the quasiparticle weight or the residual interactions of the nodal excitations. This is because the entropy counts the number of degrees of freedom that are thermally excited within an energy range of approximately $\mathbf{k}_B T$. To put this argument on a more concrete footing, we turn to an alternative calculation.

Fermi Liquid Approach to the Specific Heat of a Weyl Fermion

Adopting the Fermi-liquid approach for calculating the entropy, as outlined in ref. 6 (chapter 4, section 19), we express the specific heat per unit volume from a Weyl fermion as

$$c_v = \int\frac{d^3\mathbf{k}}{(2\pi)^2}\frac{1}{2\pi i T}\int_{-\infty}^{\infty}\varepsilon\left[-\frac{\partial f(\varepsilon)}{\partial\varepsilon}\right]\left[\ln G_R(\mathbf{k},\varepsilon) - \ln G_A(\mathbf{k},\varepsilon)\right]d\varepsilon, \quad \textbf{[S30]}$$

where T is the temperature, k_B is the Boltzmann constant, and $f(\varepsilon)$ is the Fermi distribution function. In addition, $G_R(\mathbf{k},\varepsilon) = Z/(\varepsilon - \xi_{\mathbf{k}} + i0^+)$ is the retarded Green function of Fermi liquid quasiparticles, with Z being the quasiparticle weight, and $\xi_{\mathbf{k}} = \hbar v^*|\mathbf{k}| \equiv \hbar v^* k$ for $\xi_{\mathbf{k}} > 0$ ($\xi_{\mathbf{k}} = -\hbar v^* k$ for $\xi_{\mathbf{k}} < 0$), i.e., a Weyl fermion dispersion. Likewise, the advanced Green function is $G_A = G_R^*$, and we set the chemical potential $\mu = 0$, sitting exactly at the nodal point. We use the Sommerfeld expansion

$$\int_{-\infty}^{\infty}d\varepsilon u(\varepsilon)\left[\frac{\partial f(\varepsilon)}{\partial\varepsilon}\right] \simeq -u(0) - \frac{\pi^2}{6}(k_B T)^2\left(\frac{\partial^2 u(\varepsilon)}{\partial\varepsilon^2}\right)_{\varepsilon=0} - \frac{7\pi^4}{360}(k_B T)^4\left(\frac{\partial^4 u(\varepsilon)}{\partial\varepsilon^4}\right)_{\varepsilon=0} + \cdots. \quad \textbf{[S31]}$$

Taking derivatives and setting $\varepsilon = 0$, we obtain

$$c_v = \int\frac{d^3\mathbf{k}}{(2\pi)^3}k_B\left[\frac{\pi}{3}k_B T\, Im\left(G_R^{-1}\partial_\varepsilon G_R\right)_{\varepsilon=0} + \frac{7\pi^4}{90}(k_B T)^3 Im\left(G_R^{-1}\partial_\varepsilon^3 G_R + 2G_R^{-3}(\partial_\varepsilon G_R)^3 - 3G_R^{-2}\partial_\varepsilon G_R\partial_\epsilon^2 G_R\right)_{\varepsilon=0}\right], \quad \textbf{[S32]}$$

where $Im\,(A)$ means the imaginary part of A. For a Weyl fermion, we find that $Im\left[G_R^{-1}\partial_\varepsilon G_R\right] = \pi\delta(\varepsilon - \xi_{\mathbf{k}})$, where $\delta(x)$ is the Dirac delta function; the identity

$$\frac{1}{x+i0^+} = \mathcal{P}_v\left(\frac{1}{x}\right) - i\pi\delta(x) \quad \textbf{[S33]}$$

has been used, with $\mathcal{P}_v$ denoting principal value. For the leading linear-T term, the integral involves

$$\int\frac{4\pi k^2 dk}{(2\pi)^3}\delta(\xi_{\mathbf{k}}) = 0, \quad \textbf{[S34]}$$

and, therefore, the leading linear-in-T term vanishes. For the second term above, we find that

$$\begin{aligned} &G_R^{-1}\partial_\varepsilon^3 G_R + 2G_R^{-3}(\partial_\varepsilon G_R)^3 - 3G_R^{-2}\partial_\varepsilon G_R\partial_\varepsilon^2 G_R \\ &= -2\left[\mathcal{P}_v\left(\frac{1}{\varepsilon-\xi_{\mathbf{k}}}\right) - i\pi\delta(\varepsilon-\xi_{\mathbf{k}})\right]^3 \\ &= -2\left[\mathcal{P}_v\left(\frac{1}{\varepsilon-\xi_{\mathbf{k}}}\right)^3 + 3\mathcal{P}_v\left(\frac{1}{\varepsilon-\xi_{\mathbf{k}}}\right)^2(-i\pi)\delta(\varepsilon-\xi_{\mathbf{k}}) \right. \\ &\quad \left. +3\mathcal{P}_v\left(\frac{1}{\varepsilon-\xi_{\mathbf{k}}}\right)(-i\pi)^2\delta^2(\varepsilon-\xi_{\mathbf{k}}) + (-i\pi\delta(\varepsilon-\xi_{\mathbf{k}}))^3\right]. \end{aligned} \quad \textbf{[S35]}$$

Focusing on the imaginary terms, we find that only the second term in Eq. **S35** contributes to the results. The last term vanishes because the integral of cubic delta function is zero. Therefore, we find that

$$Im\left(G_R^{-1}\partial_\varepsilon^3 G_R + 2G_R^{-3}(\partial_\varepsilon G_R)^3 - 3G_R^{-2}\partial_\varepsilon G_R \partial_\epsilon^2 G_R\right)_{\varepsilon=0} = 6\pi\mathcal{P}_v\left(\frac{1}{\xi_{\mathbf{k}}}\right)^2\delta(\xi_{\mathbf{k}}). \quad \textbf{[S36]}$$

Combining all these, we obtain the specific heat per unit volume as

$$c_v \simeq \frac{7\pi^4}{15}k_B(k_B T)^3\int\frac{d^3\mathbf{k}}{(2\pi)^3}\mathcal{P}_v\left(\frac{1}{\xi_{\mathbf{k}}}\right)^2\delta(\xi_{\mathbf{k}}) \quad \textbf{[S37]}$$

$$= \frac{7\pi^4}{90}k_B(k_B T)^3\frac{1}{2}\int_{-\infty}^{\infty}\frac{4\pi k^2 dk}{(2\pi)^3}\frac{2}{(\hbar v^* k)^2}\delta(\hbar v^* k) \quad \textbf{[S38]}$$

$$= \frac{7\pi^2}{30}k_B\left(\frac{k_B T}{\hbar v^*}\right)^3, \quad \textbf{[S39]}$$

i.e., the same expression as in Eq. **S29**. It is worth noting that (*i*) the principal value evaluation is not necessary since the $\mathbf{k}^2$ in the denominator cancel the $\mathbf{k}^2$ from the numerator; (*ii*) the factor $1/2$ in front of the integral in Eq. **S38** is due to the extension of integration range from $-\infty$ to $+\infty$ while recognizing that the function is even; and (*iii*) the factor of 2 in the numerator of $2/(\hbar v^* k)^2$ inside the integral in Eq. **S38** is originated from the fact that, for each momentum k, there are two contribution from $\xi_{\mathbf{k}} = \pm\hbar v^* k$ in the Weyl fermion band distribution.

In summary, the Fermi liquid analysis here demonstrates that, even when the Fermi-liquid effects (the quasiparticle weight and residual interactions of the nodal excitations) are explicitly taken into account, the leading renormalization effect to the specific heat is still for the T^3 coefficient and has the form $(1/v^*)^3$.

1. Hewson AC (1993) The Kondo Problem to Heavy Fermions (Cambridge Univ Press, Cambridge, UK).
2. Feng XY, Dai J, Chung CH, Si Q (2013) Competing topological and kondo insulator phases on a honeycomb lattice. *Phys Rev Lett* 111:016402.
3. Volovik GE (1987) Zeros in the fermion spectrum in superfluid systems as diabolical points. *JETP Lett* 46:98.
4. Bernevig BA, Hughes TL (2013) Topological Insulators and Topological Superconductors (Princeton Univ Press, Princeton).
5. Ojanen T (2013) Helical Fermi arcs and surface states in time-reversal invariant Weyl semimetals. *Phys Rev B* 87:245112.
6. Abrikosov AA, Gorkov LP, Dzyaloshinski IE (1975) Methods of Quantum Field Theory in Statistical Physics (Dover, Mineola, NY).

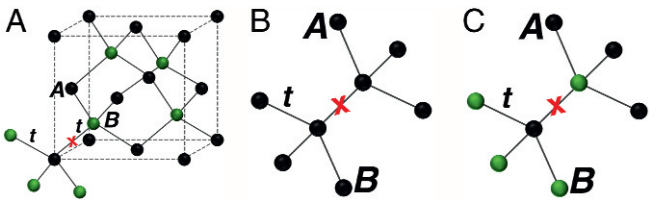

Fig. S1. (*A*) Zincblende lattice: diamond lattice with $\pm m$ differentiating *A*, *B* sublattice. (*B*) Diamond lattice unit cell. (*C*) Zincblende unit cell. Translating an *A* atom across the inversion point marked X exchanges it with the B site, breaking inversion symmetry in *A* and *C*, but preserving it in *B*, since the two sites are equivalent.

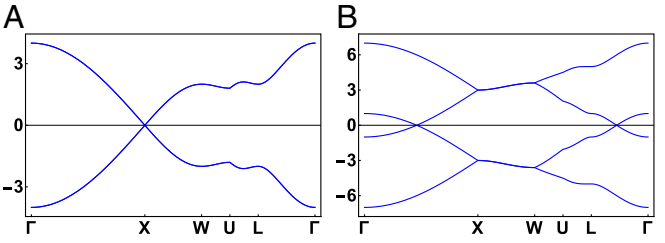

Fig. S2. Band structure along the high symmetry points of the fcc BZ in the presence of TRB (preserving inversion symmetry), originated from a local moment field M_z coupled to the conduction electron spin, using $\lambda = \frac{1}{2}$. (*A*) $M_z = 0$: Dirac semimetal. (*B*) $M_z = 3$: Weyl nodes along different lines are all moved toward Γ point.